

YOLO-CL cluster detection in the Rubin/LSST DC2 simulations

Kirill Grishin¹, Simona Mei^{1,2}, Stephane Ilic³, Michel Aguena¹, Dominique Boutigny⁴, Marie Paturel⁴, and the LSST Dark Energy Science Collaboration

¹ Université Paris Cité, CNRS/IN2P3, Astroparticule et Cosmologie, F-75013 Paris, France e-mail: grishin@apc.in2p3.fr, mei@apc.in2p3.fr

² Jet Propulsion Laboratory and Cahill Center for Astronomy & Astrophysics, California Institute of Technology, 4800 Oak Grove Drive, Pasadena, California 91011, USA

³ IJCLab, Université Paris-Saclay, CNRS/IN2P3, IJCLab, 91405 Orsay, France

⁴ LAPP, Université Savoie Mont Blanc, CNRS/IN2P3, Annecy; France

ABSTRACT

The next generation large ground-based telescopes like the Vera Rubin Telescope Legacy Survey of Space and Time (LSST) and space missions like Euclid and the Nancy Roman Space Telescope will deliver wide area imaging surveys at unprecedented depth. In particular, LSST will provide galaxy cluster catalogs up to $z \sim 1$ that can be used to constrain cosmological models once their selection function is well-understood. Machine learning based cluster detection algorithms can be applied directly on images to circumvent systematics due to models, and photometric and photometric redshift catalogs. In this work, we have applied the deep convolutional network YOLO for CLuster detection (YOLO-CL) to LSST simulations from the Dark Energy Science Collaboration Data Challenge 2 (DC2), and characterized the LSST YOLO-CL cluster selection function. We have trained and validated the network on images from a hybrid sample of (1) clusters observed in the Sloan Digital Sky Survey and detected with the red-sequence Matched-filter Probabilistic Percolation, and (2) dark matter haloes with masses $M_{200c} > 10^{14} M_{\odot}$ from the DC2 simulation, resampled to the SDSS resolution. We quantify the completeness and purity of the YOLO-CL cluster catalog with respect to DC2 haloes with $M_{200c} > 10^{14} M_{\odot}$. The YOLO-CL cluster catalog is 100% and 94% complete for halo mass $M_{200c} > 10^{14.6} M_{\odot}$ at $0.2 < z < 0.8$, and $M_{200c} > 10^{14} M_{\odot}$ and redshift $z \lesssim 1$, respectively, with only 6% false positive detections. We find that all the false positive detections are dark matter haloes with $10^{13.4} M_{\odot} \lesssim M_{200c} \lesssim 10^{14} M_{\odot}$, which corresponds to galaxy groups. We also found that the YOLO-CL selection function is almost flat with respect to the halo mass at $0.2 \lesssim z \lesssim 0.9$. The overall performance of YOLO-CL is comparable or better than other cluster detection methods used for current and future optical and infrared surveys. YOLO-CL shows better completeness for low mass clusters when compared to current detections based on Matched Filter cluster finding algorithms applied to Stage 3 surveys using the Sunyaev Zel'dovich effect, such as SPT-3G, and detects clusters at higher redshifts than X-ray-based catalogs. Future complementary cluster catalogs detected with the Sunyaev Zel'dovich effect will reach similar mass depth and will be directly comparable with optical cluster detections in LSST, providing cluster catalogs with unprecedented coverage in area, redshift and cluster properties. The strong advantage of YOLO-CL over traditional galaxy cluster detection techniques is that it works directly on images and does not require photometric and photometric redshift catalogs, nor does it need to mask stellar sources and artifacts.

Key words. Clusters – Cosmology – Machine learning

1. Introduction

Galaxy clusters are the largest gravitationally bound structures in the Universe, and their distribution is a probe for cosmological models. Upcoming deep large-scale survey like those performed with the Vera C. Rubin Observatory (Kahn 2018), the Euclid space telescope (Laureijs et al. 2011) and the Nancy Grace Roman Space Telescope (Eifler et al. 2021) will give us unprecedented deep optical and infrared imaging of hundreds of thousands of clusters up to $z \sim 2$.

In particular, the Vera Rubin Telescope Legacy Survey of Space and Time (LSST; LSST Science Collaboration et al. 2009; Ivezić et al. 2019) will deliver deep optical imaging data over $\sim 20,000$ sq. deg. of the sky. LSST will observe in six bandpasses (u, g, r, i, z, y) and reach a depth of $r \sim 27.5$ mag on about half of the sky (Olivier et al. 2012, 2006). These observations will permit us to obtain constraints on cosmological models using galaxy clusters, once we can provide a precise selection function.

Cluster detection in optical and near-infrared multi-wavelength imaging surveys is mainly based on the search of spatial overdensities of galaxies of a given class, which can

be quiescent, line-emitter, massive, etc. (e.g., Gladders & Yee 2005; Koester et al. 2007; Knobel et al. 2009; Wen et al. 2009, 2012; Sobral et al. 2010; Hao et al. 2010; Szabo et al. 2011; Muzzin et al. 2012; Bayliss et al. 2011; Wylezalek et al. 2013, 2014; Rykoff et al. 2014; Mei et al. 2015; Licitra et al. 2016a,b; Maturi et al. 2019; Werner et al. 2023). Most of these methods require a high-quality photometric calibration, an accurate calibration of galaxy colors as a function of redshift, and unbiased photometric and photometric redshift catalogs. Photometric catalogs might be affected by aperture or model choices in measuring magnitudes and background subtraction. These systematics propagate to the estimation of photometric redshifts, which also rely on being calibrated on available spectroscopic redshift samples and galaxy spectral energy distribution templates that do not cover the entire galaxy population (e.g., Moskowitz et al. 2024). These uncertainties on both photometric and photometric redshift catalogs make it essential to complement traditional cluster detection algorithms with new techniques that do not rely on catalogs, but instead work directly on images, such as deep machine learning (ML) neural network.

Over the last years, deep ML techniques were widely used in astrophysics for different purposes (Huertas-Company & Lanusse 2023), including object classification (Domínguez Sánchez et al. 2018; Angora et al. 2023), estimation of redshift of individual galaxies (Pasquet et al. 2019; Henghes et al. 2021), solution of ill-posed problems, including reconstructions of matter distributions (Jeffrey et al. 2020; Cornu et al. 2022; Chen et al. 2023). The purity of the samples, defined as the percentage of true objects recovered by the network as opposite to false detections, was high enough to search for rare or elusive objects (Hezaveh et al. 2017; Cornu & Montillaud 2021). Among these methods, convolutional neural networks (CNN) are well adapted for object detection and characterization in astrophysics (e.g., Huertas-Company et al. 2015, 2018; Dimauro et al. 2018; Pasquet et al. 2019; Zanisi et al. 2021; Euclid Collaboration et al. 2022; Davidzon et al. 2022; Euclid Collaboration et al. 2023a,b), in particular for galaxy cluster detection (e.g., Chan & Stott 2019; Bonjean 2020; Hurier et al. 2021; Lin et al. 2021; Grishin et al. 2023).

Recently, our team developed a cluster detection method modifying the well-known detection-oriented deep machine learning neural network “You only look once” (YOLO, Redmon et al. 2015; Redmon & Farhadi 2016). Our network, YOLO-CL (YOLO for CLuster detection; Grishin et al. 2023), detects galaxy clusters on multi-wavelength images, and shows a higher performance with respect to traditional cluster detection algorithms in obtaining cluster catalogs with high completeness and purity. When applied to the Sloan Digital Sky Survey (SDSS; York et al. 2000), YOLO-CL provides cluster catalogs that are complete at $\sim 98\%$ for X-ray detected clusters with $I_{X,500} \gtrsim 20 \times 10^{-15} \text{ erg/s/cm}^2/\text{arcmin}^2$ at $0.2 \lesssim z \lesssim 0.6$, and of $\sim 100\%$ for clusters with $I_{X,500} \gtrsim 30 \times 10^{-15} \text{ erg/s/cm}^2/\text{arcmin}^2$ at $0.3 \lesssim z \lesssim 0.6$. The contamination from false detections is $\sim 2\%$. It is also interesting that Grishin et al. (2023) found the YOLO-CL selection function is flat as a function of redshift, with respect to the X-ray mean surface brightness. The advantage of YOLO-CL, and other ML networks that work directly on images, is that they are independent of models and systematics that might arise when building photometric and photometric redshift catalogs in traditional methods. They also do not need stellar sources and artifacts to be masked. If the training sample is representative of the entire observed sample, the ML methods should be less impacted by modeling choices and systematics.

In this paper, we evaluate the YOLO-CL efficiency in detecting galaxy clusters in the LSST survey. Given that LSST observations did not start yet, we apply the network on simulations from the LSST Data Challenge 2 (DC2; LSST Dark Energy Science Collaboration (LSST DESC) et al. 2021), which were developed within the LSST Dark Energy Science Collaboration (DESC¹). We quantify the YOLO-CL cluster catalog selection function in terms of completeness and purity (see below) with respect to DC2 haloes with $M_{200c} > 10^{14} M_{\odot}$. The YOLO-CL cluster catalog is 100% and 94% complete for halo mass $M_{200c} > 10^{14.6} M_{\odot}$ at $0.2 < z < 0.8$, and 94% complete for $M_{200c} > 10^{14} M_{\odot}$ and redshift $z \lesssim 1$, respectively, with only 6% false positive detections. This contamination is expected from the intrinsic accuracy of convolutional neural networks, and our network is highly efficient with respect to traditional cluster detection algorithms based on photometric and photometric redshift catalogs. It is interesting that all the false positive detections are groups with $10^{13.4} M_{\odot} \lesssim M_{200c} \lesssim 10^{14} M_{\odot}$, and that the catalog selection function is flat with respect to the halo mass at $0.2 \lesssim z \lesssim 0.9$.

¹ <https://lsstdesc.org/>

This article is organized as it follows: in Section 2.2 we describe the observations and simulations used to train and validate our network. In Section 3 we present YOLO-CL and its training and validation. The results and the discussion and conclusions are presented in Section 4 and Section 5, respectively. The summary is in Sec. 6. All magnitudes are given in the AB system (Oke & Gunn 1983; Sirianni et al. 2005). We adopt a Λ CDM cosmology, with $\Omega_M = 0.3$, $\Omega_{\Lambda} = 0.7$, $h = 0.72$, and $\sigma_8 = 0.8$.

2. Observations and simulations

Since the DESC DC2 simulated area includes only $\approx 2,000$ synthetic galaxy clusters (see Sec. 2.2) and we need at least 10,000 objects for training our network, we trained YOLO-CL on a hybrid sample of cluster images that includes both the same set of SDSS observed images (Abazajian et al. 2009) that we used in Grishin et al. (2023), and synthetic cluster images from the DESC DC2 simulations.

This strategy is widely used in astrophysics when the target sample (in our case the LSST DC2 simulations) is large enough to provide a statistical application of a network, but too small to be used for the network training and validation. In the case of convolutional networks, such as YOLO-CL, Domínguez Sánchez et al. (2018) demonstrated that transfer learning allows for rapid adaptation from one astrophysical survey application to another. Specifically, the weights obtained by training a convolutional network on images from a given survey can be efficiently transferred to another survey by fine-tuning them, i.e., by retraining the network adding a smaller number of images from the new survey, roughly an order of magnitude fewer than the initial training sample. In their case, the initial survey was SDSS, and they applied transfer learning to the Dark Energy Survey (Abbott et al. 2018). We demonstrate in this section that this approach is also effective when re-training YOLO-CL using our initial training set from SDSS as utilized in Grishin et al. (2023), and incorporating approximately one order of magnitude fewer synthetic cluster images from the DESC DC2 simulations.

2.1. The SDSS observations

The SDSS is an imaging survey that was performed with the 2.5-m. Apache Point telescope in five optical bandpasses (u, g, r, i, z) using the SDSS camera in a scanning regime. It covers $\sim 14,055 \text{ sq. deg.}$ of the sky in two main areas in the Northern hemisphere split by the Milky Way: one within $7\text{h} < \text{RA} < 16\text{h}$ and $-1 \text{ deg} < \text{Dec} < +62 \text{ deg.}$ and the other within $20\text{h} < \text{RA} < 2\text{h}$ and $-11 \text{ deg.} < \text{Dec} < +35 \text{ deg.}$ The $5\text{-}\sigma$ point-source depth in the g, r and i bandpasses is 23.13, 22.70 and 22.20 mag, respectively. The seeing quality for SDSS images varies from 1.2 to 2.0 arcsec².

As reference SDSS cluster catalog, we used the red-sequence Matched-filter Probabilistic Percolation (redMaPPer) Data Release 8 (DR8) catalog from Rykoff et al. (2014). The redMaPPer algorithm finds overdensities of red sequence galaxies in large photometric surveys. The cluster catalog that we used³ covers $\sim 10,000$ square degrees of the SDSS DR8 data release, and includes 26,111 clusters over the redshift range $z \in [0.08, 0.55]$. The redMaPPer catalog is 100% complete up to $z = 0.35$ for clusters from the MCXC (Meta-Catalog of X-Ray Detected Clusters of Galaxies) X-ray detection catalog (Piffaretti et al. 2011), with temperature $T_X \gtrsim 3.5 \text{ keV}$, and luminosity $L_X \gtrsim$

² https://www.sdss4.org/dr17/imaging/other_info/

³ Version 6.3 of the catalog, from risa.stanford.edu/redMaPPer.

2×10^{44} erg s⁻¹, decreasing to 90% completeness at $L_X \sim 10^{43}$ erg s⁻¹. The centers of 86% of the redMaPPer clusters correspond well to their X-ray centers (Rykoff et al. 2014). For each cluster, redMaPPer provides its position, the richness λ^4 , and a list of cluster members. The richness is correlated to the cluster mass. All redMaPPer rich clusters ($\lambda > 100$) are detected in the X-ray ROSAT All Sky Survey (Voges et al. 1999).

We excluded clusters with redshifts $z < 0.2$ from the original redMaPPer cluster catalog, because they cover regions in the sky larger than the images that we consider when optimizing our network execution time and computational power (see sec. 3.2). Our final redMaPPer catalog includes 24,406 clusters, whose distribution is shown in Fig. 1 from Grishin et al. (2023).

For the network training and validation, we used JPEG color images of the original SDSS DR16 images centered on each of the 24,406 redMaPPer clusters, using the ImgCutout web service⁵. These images were derived from the g , r , and i -band FITS corrected frame files from the Science Archive Server, and the color images are built using the conversion algorithm⁶ based on Lupton et al. (2004). We chose these three bandpasses because they are sufficient to identify passive early-type galaxies in clusters at $z \lesssim 1$.

2.2. The DESC DC2 simulation

In ten years, LSST will reach the $5\text{-}\sigma$ point-source depth of 27.4, 27.5, and 26.8 mag in the g , r and i bandpasses, respectively (Ivezić et al. 2019). This will allow to build a catalog of 20 billion individual galaxies, and over 100,000 galaxy clusters at $z < 1.2$. The average seeing quality at the Rubin telescope site is 0.67" with a best value of 0.4", which is very close to the best spatial resolution that can be achieved from the ground.

The primary goal of the LSST DESC DC2 simulation is to create realistic LSST synthetic observations that can be used to test all DESC primary pipelines. DC2 is based on the Outer Rim cosmological N-body simulation, that contains around a trillion particles in 4.225 Gpc³ of co-moving volume (Heitmann et al. 2019). An extragalactic catalog, CosmoDC2, was built from the snapshots of Outer Rim simulation by: 1) assigning galaxies to each halo of the dark matter simulation with properties obtained from empirical relations (Behroozi et al. 2019), and 2) fully characterizing galaxies in this sample adding missing properties derived from the semi-empirical model (SAM) Galacticus (Benson 2012).

The CosmoDC2 catalog was used to simulate images over an area of 445 sq. deg., with galaxies at $z < 3$. The sample of galaxies in the initial truth catalog is complete down to $r = 28.0$ mag, and galaxies fainter than $r = 29.0$ mag are excluded from the simulations for computation performance purposes. The catalog is stored in the HEALPix format (Górski et al. 2005) and split into three redshift bins: $0 < z < 1$, $1 < z < 2$ and $2 < z < 3$. The quality of this catalog was evaluated in the framework of the LSST DESC collaboration using the DESCQA validation framework (Mao et al. 2018). This validation confirmed that the simulation reproduce reasonably well galaxies, their properties, and their distribution

⁴ By definition, the cluster richness is the number of cluster members above a given luminosity. For redMaPPer it is defined as a sum of the probability of being a cluster member over all galaxies in a cluster field (Rozo et al. 2009).

⁵ <http://skyserver.sdss.org/dr16/en/help/docs/api.aspx#imgcutout>

⁶ Detailed here: <https://www.sdss.org/dr16/imaging/jpg-images-on-skyserver>

in the Universe (Kovacs et al. 2022). This makes the DC2 simulation one of the best dataset to test the DESC cosmological pipelines and algorithms, including cluster finders.

The simulation includes both a catalog and synthetic images. The simulation of the DC2 synthetic images consisted of two main steps: 1) simulation of raw images that resemble those obtained with LSSTCam, and 2) reduction of these raw images using the LSST science pipeline⁷, based on the Hyper Supreme-Cam pipeline (Bosch et al. 2018). On the first step, each object from cosmoDC2 catalog was simulated using the GalSim package (Rowe et al. 2015), taking into account the LSST depth and noise, accounting for CCD effects, night sky background (Yoachim et al. 2016), cosmic ray hits, etc. Galaxy colors and spectral energy distributions were modeled using templates from Bruzual & Charlot (2003).

The raw synthetic images were then processed by the LSST science pipeline, which covers: 1) single-frame processing, by basic corrections like bias subtraction, non-linearity and flat-field corrections, and first iteration of astrometric and photometric calibration 2) joint calibration, which uses synthetic observations of the same area of the sky from different frames to improve the calibration 3) image co-addition, when individual images are resampled on the same coordinate grid, and then coadded, and 4) source detection. The 5σ point-source depth of the simulation in the r -band is 27.3 mag, which corresponds to 5 years of the LSST survey, the deeper DC2 images on a large area currently available.

Using the Dark Energy Survey (DES; Abbott et al. 2018) exposure checker (Melchior et al. 2016), a few dozens of DESC members performed a quality check of $\sim 9,000$ synthetic co-added images, which did not show substantial issues (LSST Dark Energy Science Collaboration (LSST DESC) et al. 2021). The galaxy catalogs comply with the LSST Science Requirements (Ivezić & the LSST Science Collaboration 2013) and the DESC Science Requirements (The LSST Dark Energy Science Collaboration et al. 2018). These images are expected to have properties, including depth and seeing quality, very close to those that will be obtained with LSSTCam (Roodman et al. 2018).

The cosmoDC2 v1.1.4 catalog includes 2,342 dark matter halos with $0.2 < z < 1$ and $M_{200c} > 10^{14} M_{\odot}$ ⁸ (the typical minimal halo mass of virialization from Evrard et al. 2008 that defines galaxy clusters, hereafter we will refer to these haloes as DC2 clusters) and redshift in the range $0.2 < z < 1.0$. Hereafter, we refer to this sample as our DC2 "true cluster" sample. We exclude halos on the simulation edges, which are not entirely included in the images. In this work, we use this sample as the "true cluster" sample. Fig. 1 shows our DC2 cluster sample and its redshift and mass distributions.

For each halo, the catalog includes its position, the true redshift, the dark matter halo mass M_{200c} , and a richness parameter defined as the sum of the probabilities for galaxies brighter than $m^*(z) + 2$ to be a halo member. Here m^* is the characteristic magnitude that corresponds to the luminosity of the knee of the Press–Schechter luminosity function (Press & Schechter 1974) at the redshift of the cluster. To find m^* , we fitted the galaxy luminosity function in the K-band (Lin et al. 2006). Then, we predict m^* in optical bands using the PEGASE2 library (Fioc & Rocca-Volmerange 1999) for a burst galaxy that passively

⁷ <https://pipelines.lsst.io/>

⁸ M_{200c} is defined as the mass within the circular region of radius R_{200} containing a mean mass density equal to two hundred times the critical density of the Universe at a given redshift.

evolves from $z=3$. The probability for the galaxy to be a cluster member was computed assigning a weight depending on the projected distance from the cluster center following Rykoff et al. (2012, 2014).

To generate composite color images, we used the DEEP-COADD frames delivered by the LSST pipeline in the DC2 Run2.2 simulation run (LSST Dark Energy Science Collaboration (LSST DESC) et al. 2021) for the cosmoDC2 v1.1.4 extragalactic catalog (Korytov et al. 2019). These images are fully reduced, calibrated, sky subtracted and co-added science frames with a pixel scale of $0.2''/\text{pix}$. To make our analysis fully consistent with the SDSS images, we have resampled the DC2 images to the SDSS pixel scale of $0.39''/\text{pix}$ using the astropy-based REPROJECT package (Robitaille et al. 2020).

To build composite JPEG color images for DC2 simulation we used the same algorithm used in the SDSS survey (Lupton et al. 2001). This algorithm has two main parameters: nonlinearity (Q) and flux scale (α). For SDSS, the parameters are $Q=8$ and $\alpha=0.2^9$. For the DC2 color images, we used $Q=8$ and $\alpha=0.08$, in order to partially compensate the depth and magnitude zero-point difference (the zero magnitudes are $m_0^{SDSS} = 22.5$ mag and $m_0^{LSST} = 27$ mag). In fact, with $\alpha=0.08$, the DC2 scale visually reproduces the SDSS scale. We also adjusted the DC2 flux count range to have a similar range in surface brightness as in SDSS. We performed a sky subtraction, and registered the composite images on a final JPEG scale from 0 to 255. We set to zero and 255 all pixels with fluxes less than zero and larger than 255, respectively.

3. YOLO-CL training and validation

3.1. YOLO-CL

YOLO-CL¹⁰ is based on the third iteration of YOLO, YOLOv3 (Redmon & Farhadi 2018), which represents a significant improvement over the first versions, and proved to be very well adapted for cluster detection (Grishin et al. 2023). We outline here the algorithm main characteristics, and more details can be found in Grishin et al. (2023). The YOLO architecture applies a single neural network to images, combining object detection and classification into a single process. This results in several orders of magnitude faster execution times, compared to other detection convolutional networks such as R-CNN (Region Based Convolutional Neural Networks, Girshick et al. 2013, and the following developments Fast and Faster R-CNN).

The network divides the image into a $S \times S$ grid of cells, within which the detection and classification are performed. For each object detection the network predicts B bounding boxes, to which it assigns a set of parameters, including its position, size, the probability of being an object and the probability of belonging to a certain class of objects. The network is trained on a sample of images on which it optimizes the parameters to better detect and classify objects (i.e., converges on the optimal weights).

During the training process YOLO-CL optimizes a multi-component loss function \mathcal{L} (Redmon et al. 2015; Grishin et al. 2023):

$$\mathcal{L} = \mathcal{L}_{\text{obj}} + \mathcal{L}_{\text{bbox}} + \mathcal{L}_{\text{class}} . \quad (1)$$

Where \mathcal{L}_{obj} is the "objectness loss" and optimizes the object identification, $\mathcal{L}_{\text{bbox}}$ is the "bounding box loss" and optimizes the

bounding box position and size, and $\mathcal{L}_{\text{class}}$ is the "classification loss" and optimizes the object class. The loss functions quantify the distance between the true parameter values and those estimated by the network. With respect to the original YOLO "classification loss" function that considers several object classes, in YOLO-CL we removed multiple object classes because we use a single object class, which is "cluster". As "bounding box loss", we used the generalized Intersection over Union (gIoU) loss (Rezatofighi et al. 2019). In fact, the traditional IoU (Intersection over Union¹¹) metric does not permit us to optimize the corresponding loss term when the true and predicted bounding boxes are non-overlapping. More details can be found in Grishin et al. (2023).

The YOLO-CL training consists of several iterations, which are called epochs. At each epoch all the images from the training sample are an input for the network which optimizes the network weights and bias that decrease the loss function, making the distance between the true values and those estimated by the network closer. The network is then validated on a validation sample.

The final network output is a catalog of detections with an associated detection probability (see below).

3.2. Training and validation

We used two equal hybrid samples of 12,203 redMaPPer and 1,171 DC2 cluster images each for both training and validating YOLO-CL, with the same number but different images for the training and validation. Each of these two samples has identical redshift and mass distribution, for a total of 24,406 redMaPPer and 2,342 DC2 cluster images. Our hybrid training and validation sample approach makes the YOLO-CL learning invariant to the differences in object densities, and all the other differences between SDSS and DC2.

Following Grishin et al. (2023), we start with images of dimension 2048×2048 pixels, which corresponds to $\sim 13.5 \times 13.5$ arcmin², twice the size of a typical cluster virial radius of 1 Mpc at $z \sim 0.2$, and much larger than the typical cluster virial radius at $z > 0.5$. For the input to the first layer of the network, we resize each image by average pooling to 512×512 pixels (with a pixel size equal to eight times the LSST resolution¹²) and 1024×1024 pixels (with a pixel size equal to the four times of the LSST resolution¹³), and keep the same stride parameters as in the original YOLOv3 publication, namely 8, 16, and 32.

These image sizes and stride parameters are a good compromise between keeping high image resolution and our computational power. Our training and validation runs were performed on Centre de Calcul IN2P3¹⁴ computing cluster on a NVIDIA Tesla V100-SXM2-32GB GPU, equipped with 32 GB of memory.

3.2.1. Hyperparameter optimization

Our hyperparameters optimization is performed with respect to memory limits and the stability of the training. Since the weight optimization during the training is done using a gradient descent, the whole process can be a subject to instabilities. There are two main hyper-parameters responsible for the mitigation of these instabilities: the batch size and the learning rate. The size of the

¹¹ The IoU is defined as the ratio between the area of intersection and the area of union between the detected object bounding box and the "true object" bounding box (Redmon et al. 2015)

¹² four times the SDSS resolution

¹³ the double of the SDSS resolution

¹⁴ <https://cc.in2p3.fr/>

⁹ <https://sdss4.org/dr17/imaging/jpg-images-on-skyserver/>

¹⁰ GITHUB PAGE

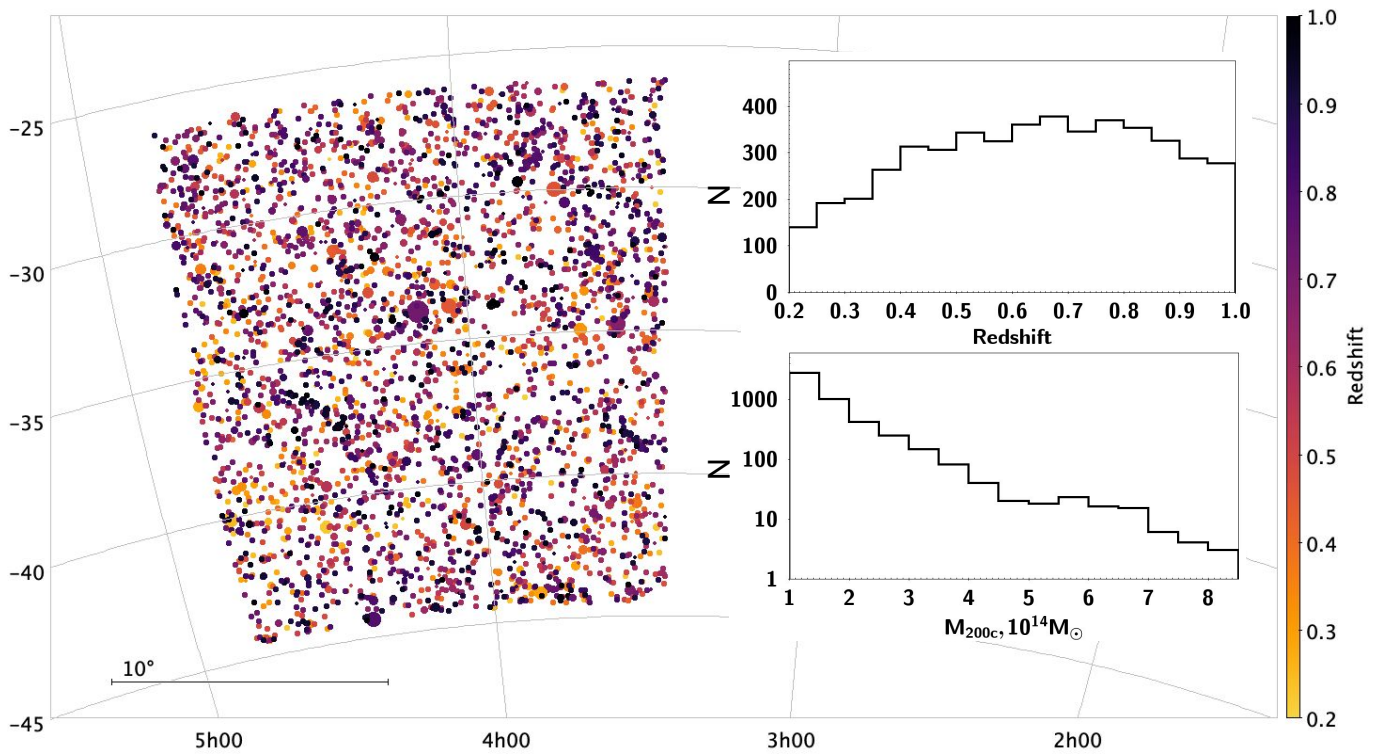


Fig. 1. Sky map with the positions of the 2,342 total CosmoDC2 clusters with $M_{200c} > 10^{14} M_{\odot}$ that we used for the YOLO-CL training and validation. Larger circle sizes indicate larger masses, and redshift is coded by color, as indicated in the right bar). In the insert: the dark matter halo redshift and mass distributions.

Table 1. Settings used for the YOLO-CL training

Image resolution	Batch size	Number of training epochs	Data augmentation technique	Augmentation frequency per technique	gIoU threshold
1024×1024	2	100	horizontal flip, vertical flip, transpose, translate	50 %	50 %
512×512	8	100	horizontal flip, vertical flip, transpose, translate	50 %	50 %

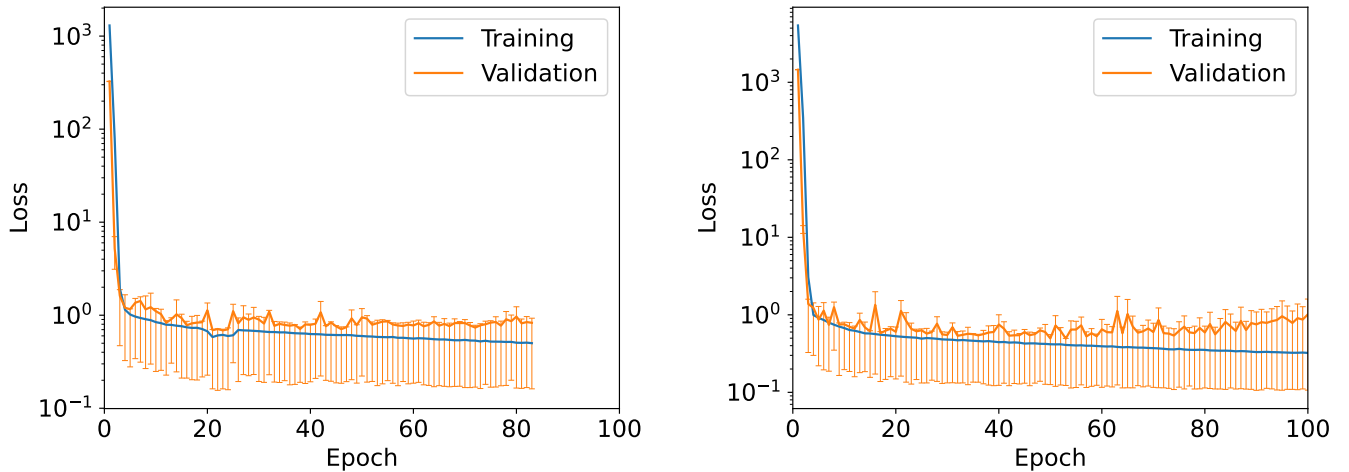


Fig. 2. The YOLO-CL loss functions for the training (blue) and validation (orange) samples, for the 512x512 (left) and 1024x1024 (right) images. The vertical bars show the 1σ standard deviation of the validation loss. The training and validation loss functions converge in a smooth way, and their good agreement confirms the network stability in both cases.

training sample is too large to store in memory, and it is not possible to complete the training on the entire sample in one iteration. To overcome this limitation, we split our training sample in subsets (batches) that are processed by the network at the same

time. The batch size is limited by two main factors: it cannot be too small, because in this case the derived direction of the gradient would be unstable, and at the same time it cannot be too big, given that memory resources are limited. Due to memory limita-

tions, we used a batch size of 8 for the 512x512 images and of 2 for the 1024x1024 images.

The other hyper-parameter that is crucial for training is the learning rate. It defines how big the weight variations can be at each epoch. It cannot be too small, otherwise the most optimal weight configuration would never be achieved, and it cannot be too big because it would make the training process less stable. We choose the learning rate varying with the epoch: it starts from a some small value and grows up during a few first epochs, called “warm-up” epochs, and after reaching its maximum values it asymptotically goes down to the final values (Grishin et al. 2023). Starting, maximal and final values of the learning rate as well as the number of “warm-up” epochs are also hyper-parameters, and should be defined before the training. We start by setting a learning rate of 10^{-10} , which grows to 10^{-5} during the first eight warm-up epochs, and then slowly decreases to 10^{-6} .

Our input image cutouts are centered on the redMaPPer cluster or DC2 selected dark matter halo positions. This centering should not have an impact on the network learning, which should understand that cluster features should not depend on its position in the image. For this reason, we apply data augmentation, including translation and flipping of a random quantity between zero and half of the image, which change the initial cluster position in the image. This forces the network to focus on the relevant features associated with clusters, independently of their position in the images.

We provide the main parameters of the training configuration in Table 1.

4. Results

4.1. Network initial detection catalog

We run YOLO-CL on the training and validation sample for ~ 100 epochs. Fig. 2 shows the loss functions for the two samples with different image size. For both cases the training epochs can be split into three parts: 1) in the first epochs the weights converge fast towards optimal values due to the large value of the gradient, 2) the search for an optimal loss minimum (epochs 10-40) and 3) the fine-tuning of the solution. In both cases the lowest value of the validation loss function is reached in the first half of the training epochs – for 512x512 it was in the range of epochs 10-45, and for 1024x1024 in the range 10-30.

At each epoch, the network output is a catalog of detections on the validation sample, with the bounding box coordinates, and the probability to belong to the class “cluster” (hereafter detection probability). The network usually outputs multiple detections of the same object, which we discard by following the standard approach in YOLO applications (Redmon et al. 2015; Redmon & Farhadi 2018). In this case, we define the IoU as the ratio between the area of intersection and the area of union between multiple detection bounding boxes. The gIoU is an optimization of the IoU (see sec. 3.1; Rezatofighi et al. 2019), and is defined as:

$$\text{gIoU} = \text{IoU} + \frac{\mathcal{U}}{\mathcal{A}_c} - 1 \quad (2)$$

where \mathcal{U} and \mathcal{A}_c are the areas of the union of the two boxes and the smallest box enclosing both boxes, respectively.

Both the IoU and gIoU are a measurement of the overlap region of bounding boxes that define two different detections. A value of 1 indicates perfect agreement (we are detecting the same object), while a value approaching 0 indicates increasingly

disjointed boxes and/or significantly different sizes (we are detecting different objects). We discard multiple detections of the same object by applying a gIoU threshold of 0.5, which is the same threshold as in the original YOLO for the IoU (Rowe et al. 2015; Redmon & Farhadi 2018). This standard choice means that when two bounding boxes overlap more than 50%, we consider that they define the same detected object. In this case, we kept the highest probability detection while discarding the other.

For each epoch, after discarding multiple detections, we obtained a catalog of single detections, each with the coordinates of the bounding box of the detection and the YOLO-CL probability of the detection being a cluster.

4.2. Final YOLO-CL cluster catalog

At this point, we needed to choose our best epoch and which probability threshold to use to select the best cluster candidates for our final YOLO-CL catalog.

Our best epoch was chosen as the epoch in which the validation loss function reaches its minimum value. This means that in this epoch we reach on average the best values of all the network parameters.

Once we chose the best epoch, to assess our best probability threshold, we used two quantities, the final cluster detection catalog completeness and purity, which are calculated on the YOLO-CL DC2 detections with respect to our reference DC2 “true cluster” sample from the simulation catalog. In fact, while we need a hybrid SDSS and DC2 sample for transfer learning, hereafter all our results will focus on the YOLO-CL performance on DC2 simulations, which are the sample on which we want to test the YOLO-CL performance on LSST, and which define our cluster catalog selection function.

The cluster catalog completeness quantifies the fraction of true clusters that are detected. The cluster catalog purity quantifies the fraction of detections that are true clusters, as opposite to false positive detections. In machine learning literature, the completeness corresponds to the recall, and the purity to the precision. To calculate the purity (see below), we applied YOLO-CL to a sample of images (“random” fields) that do not contain DC2 clusters, which means that the center of the random fields is more than 12 arcmin (~ 4.5 Mpc at $z \gtrsim 0.5$) from any DC2 cluster. For this reason, we added to our validation 6,451 random fields, which correspond to all the regions that do not contain clusters in DC2.

We optimized the detection probability threshold to obtain cluster detection catalogs with the highest values of completeness and purity. Following Grishin et al. (2023), we optimized purity and completeness to the same value, not to have one variable more optimized with respect to the other. The final YOLO-CL catalog includes only detections that have a detection probability higher than the optimized detection threshold for which completeness and purity are the same. A more fine-tuned selection function can be defined depending on the use of the catalog for cosmology, galaxy formation and evolution studies, etc.

Fig. 3 shows the catalog completeness and purity as a function of the detection probability threshold at our best epoch. The completeness $C = \frac{N_{td}}{N_{tc}}$ is calculated as the ratio between the number of true cluster detections N_{td} and the number of true clusters in our images N_{tc} . The purity is calculated as $P = 1 - \frac{N_{fd}}{N_{rf}}$, where N_{rf} is the number of random fields and N_{fd} are cluster detections in the random fields, which are by definition false positive detections. We assume that the ratio $\frac{N_{fd}}{N_{rf}}$ is a good approximation of the true ratio of false positive detections over the total number

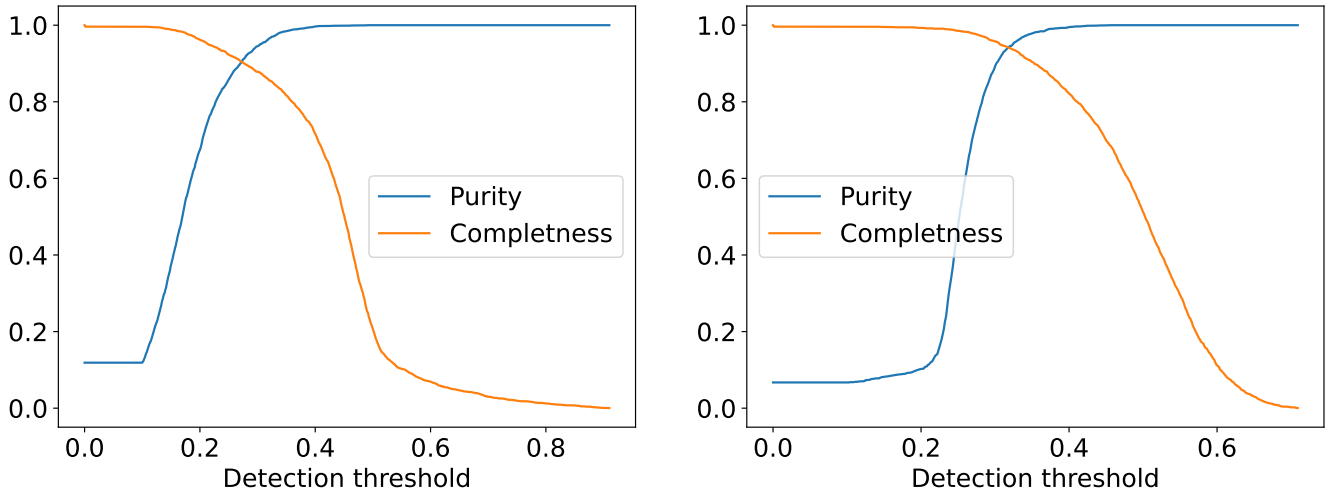


Fig. 3. The purity and completeness of the YOLO-CL DC2 detection catalogs for 512x512 (left) and 1024x1024 (right) images as a function of the detection threshold. The best purity and completeness are 90% and 94% for the 512x512 and 1024x1024 pixel images, respectively.

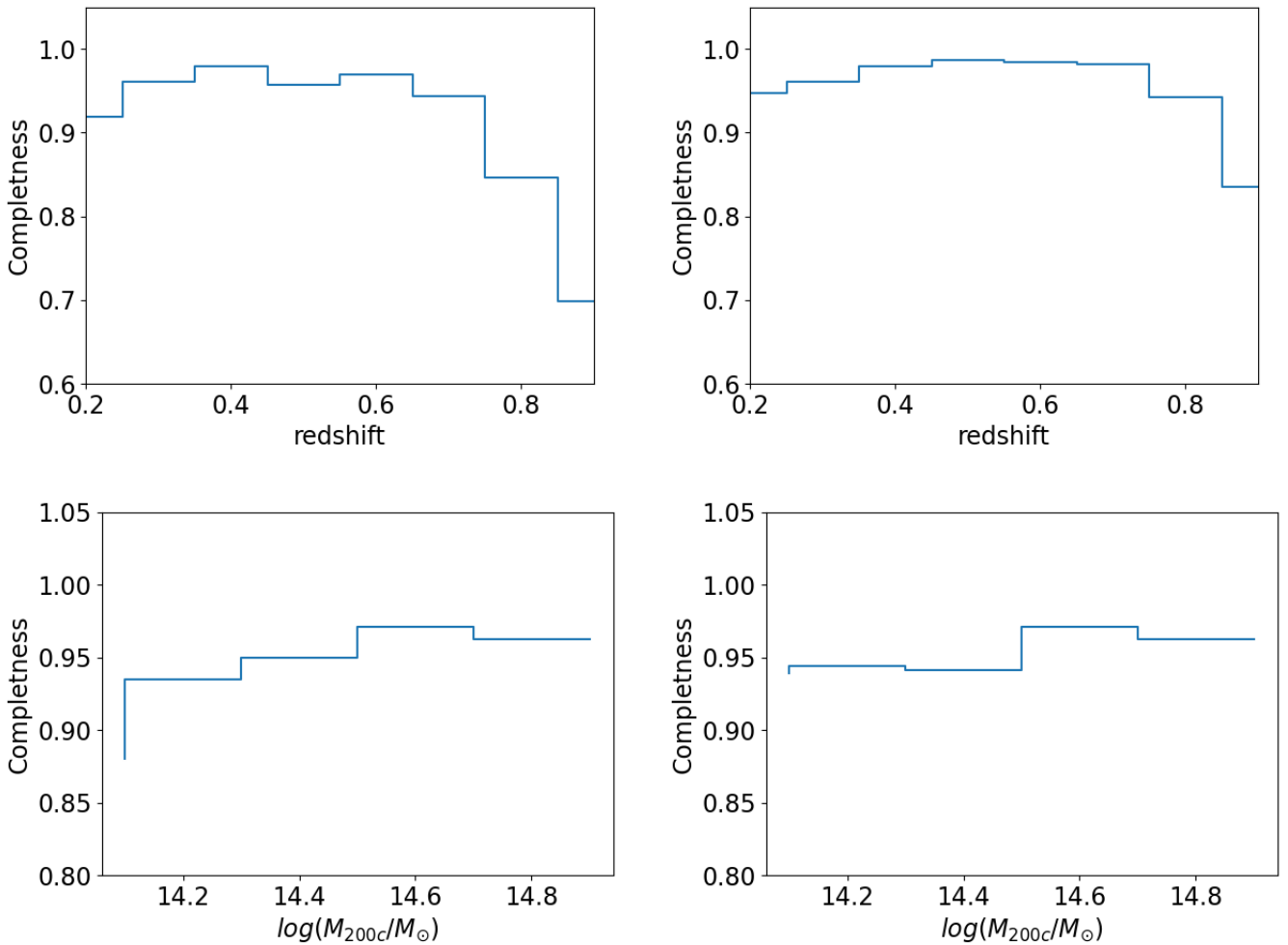


Fig. 4. The YOLO-CL DC2 detection completeness as a function of redshift (Top), and halo mass M_{200c} (Bottom) for the 512x512 (left) and 1024x1024 (right) pixel images. The completeness as a function of redshift is almost flat at the region $0.2 < z < 0.8$ with an average value of 0.85 for 512x512 and 0.95 for 1024x1024.

of detections, independently on the area of the survey that we consider. Completeness and purity have the same value of 90%

and 94% at the threshold value of 27% and 32% when using the 512x512 pixel and 1024x1024 pixel images, respectively.

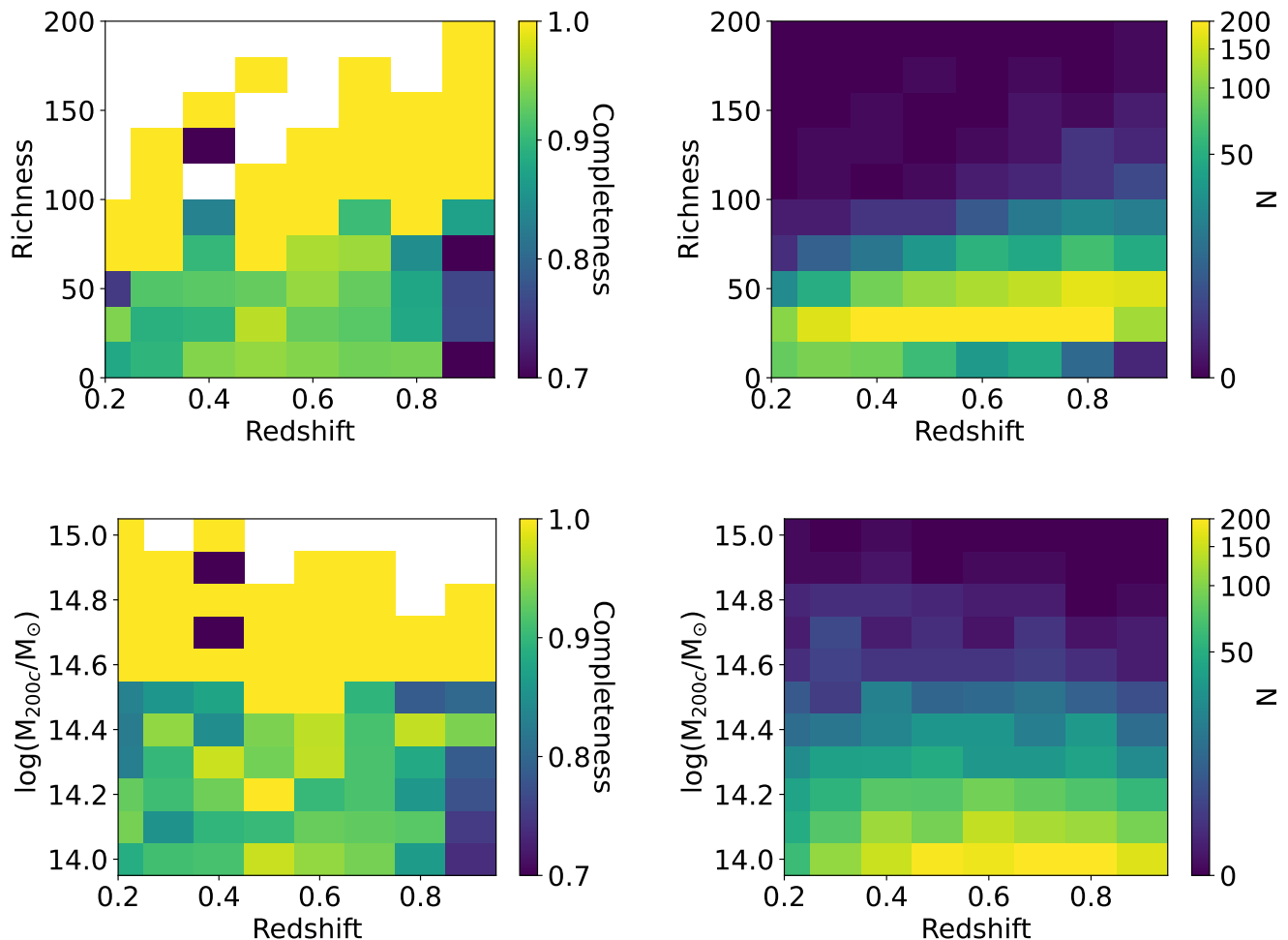


Fig. 5. Left: YOLO-CL DC2 detection completeness as a function of redshift and richness (top) or halo mass (bottom). Right: the number of halos as a function of redshift and richness (top) or halo mass (bottom). The colored vertical bars show the color scale for the completeness (left) and the number of haloes (right). The YOLO-CL selection is almost flat as a function of redshift up to $z \sim 0.8$ when we consider the halo mass. The catalog is $\sim 100\%$ complete for $M_{200c} \gtrsim 10^{14.6} M_{\odot}$ and richness $\gtrsim 100$ at all redshifts. When characterizing halos by their richness, the completeness is less flat as a function of redshift, as also shown for SDSS observations in [Grishin et al. \(2023\)](#), and the completeness decreases abruptly to $\sim 70 - 75\%$ at $z > 0.8$ and $M_{200c} \lesssim 10^{14} M_{\odot}$. Comparing the figures on the left and on the right, some bins show very low completeness on the left only because there are no clusters in those bins.

Figure 4 shows the completeness as a function of the DC2 "true cluster" mass M_{200c} and redshift. The completeness is almost flat at $0.2 < z < 0.8$ and varies in the range of 80%-90%, and 90%-96% when YOLO-CL is applied to 512x512 and 1024x1024 pixel images, respectively. At $z > 0.8$, we observe a decrease in completeness, which is larger when considering 512x512 pixel images. The completeness also increases with the halo mass. For the 512x512 pixel images the completeness is $\gtrsim 95\%$ only for halos with $M_{200c} > 10^{14.7} M_{\odot}$, while for 1024x1024 images it is $\gtrsim 94\%$ for $M_{200c} > 10^{14} M_{\odot}$.

4.3. YOLO-CL final catalog completeness and purity

Given the higher network performance with 1024x1024 pixel images, hereafter we concentrate on the catalog obtained with this image size. In this final YOLO-CL catalog, we only keep cluster candidates with detection probability higher than a 32% threshold, which corresponds to a catalog 94% complete and pure.

Fig. 5 shows the YOLO-CL detection catalog completeness as a function of both redshift and DC2 halo mass and richness. Halo mass and richness are correlated, with a large scatter, and a $M_{200c} = 10^{14} M_{\odot}$ corresponds to a richness ~ 35 . The YOLO-CL selection is almost flat with respect to the halo mass up to $z \sim 0.9$, but not with respect to richness. This might be due to the fact that the features found by the network to identify a cluster, or the non-linear combination of these features, are more linked with the cluster mass than with its richness.

The catalog is $\sim 100\%$ complete for $M_{200c} \gtrsim 10^{14.6} M_{\odot}$ and richness $\gtrsim 100$ at all redshifts. At $M_{200c} \gtrsim 10^{14} M_{\odot}$, the completeness is $\gtrsim 95\%$ up to $z \sim 0.8$, and decreases to $\gtrsim 80-85\%$ at higher redshifts. However, when characterizing halos by their richness, the completeness is less flat as a function of redshift, as also shown for SDSS observations in [Grishin et al. \(2023\)](#), and decreases abruptly to $\sim 70 - 75\%$ at $z > 0.8$.

To better understand the purity of YOLO-CL catalog as function of redshift, we matched the 6% false detections to lower mass DC2 dark matter haloes, which are the most probable interlopers. Unfortunately, we cannot estimate purity as a function

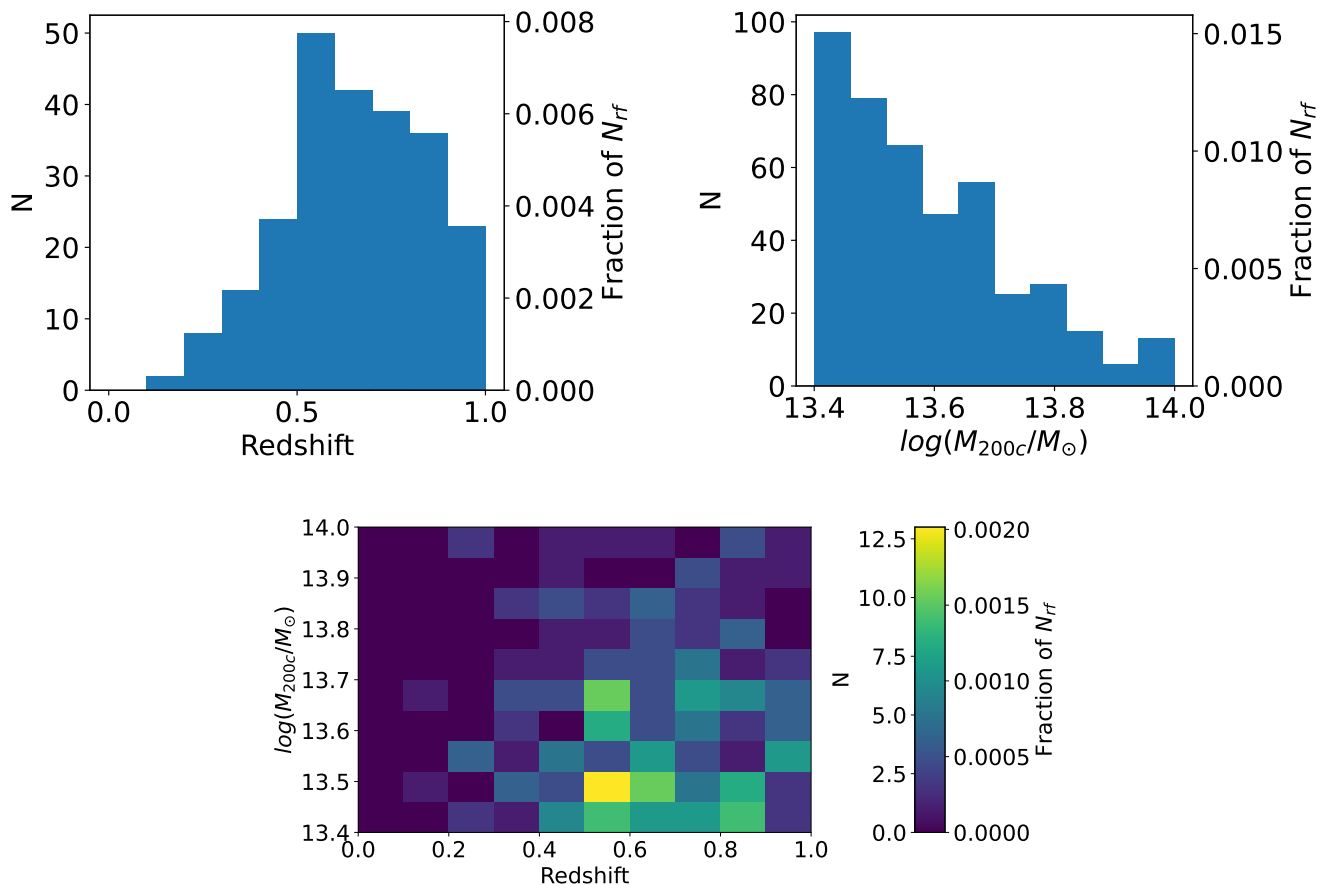


Fig. 6. Distribution of the ratio of YOLO-CL DC2 false positive detections to the total number of random fields N_{rf} as a function of halo mass and redshift (Top) and both (Bottom). In the bottom panel, the scale on the right indicates the number of false positive detections N , and the ratio of N to the total number of random fields N_{rf} . The total number of YOLO-CL random fields is 6,451.

of both mass and redshift because we would need the number of detected clusters with a given observed mass and redshift, and YOLO-CL does not provide an estimation of these parameters. We found that 49%, 97%, and 100% of the false detections match with halos $10^{13.8}M_{\odot} < M_{200c} < 10^{14}M_{\odot}$, $10^{13.5}M_{\odot} < M_{200c} < 10^{14}M_{\odot}$, and $10^{13.4}M_{\odot} < M_{200c} < 10^{14}M_{\odot}$, respectively, of which 24%, 79%, and 85% are at $z < 1$, respectively. Fig. 6 shows their distributions as a function of mass and redshift.

Most of the contamination of the final cluster sample is due to groups with $10^{13.7}M_{\odot} < M_{200c} < 10^{14}M_{\odot}$ (i.e., objects with masses within 0.3 dex smaller than a cluster) and $z \gtrsim 0.6$.

From the DES Y1 redMaPPer cluster catalog (McClintock et al. 2019), the cluster mass uncertainty is estimated to be 0.13 dex at $z \lesssim 1$ and $M_{200c} > 10^{14}M_{\odot}$ (Farahi et al. 2019). This means that our false positive detections cannot be distinguished from "true clusters" within 3σ of the current DES observational mass uncertainty, which might be taken as a hypothetical lower limit on future LSST cluster mass uncertainties.

The mass observational uncertainty would also introduce an Eddington bias, which means that the more numerous $M_{200c} < 10^{14}M_{\odot}$ haloes will be assigned a mass estimation $M_{200c} > 10^{14}M_{\odot}$, and then contaminate our cluster sample with lower mass groups. To estimate this bias and using again the current DES cluster mass uncertainty as a reference, we statistically estimated the number of groups in the DC2 footprint with $M_{200c} < 10^{14}M_{\odot}$ that may have a mass estimate of $M_{200c} > 10^{14}M_{\odot}$ due

to the scatter of the cluster mass-richness relation, and obtain an Eddington bias of 11%.

With this hypothesis, this means that 6% of the detections in the YOLO-CL cluster catalog would be groups with $10^{13.4}M_{\odot} < M_{200c} < 10^{14}M_{\odot}$, and at least $\sim 10\%$ of these groups are expected to be assigned a mass $M_{200c} > 10^{14}M_{\odot}$. In practice, in current surveys the uncertainty on halo mass at $M_{200c} < 10^{14}M_{\odot}$ is about two times larger than the uncertainty at $M_{200c} > 10^{14}M_{\odot}$, about 0.25-0.3 dex (e.g., Simet et al. 2017; Parroni et al. 2017). If that will be also true for LSST, the Eddington bias contamination will be of the order of $\sim 30\%$, and all these estimates have to be re-assessed when LSST cluster mass uncertainties will be estimated.

5. Discussion and Conclusions

Our results show that YOLO-CL detects DC2 clusters ($M_{200c} > 10^{14}M_{\odot}$) in regions centered around them with $\sim 94\%$ completeness and purity at $0.2 \lesssim z \lesssim 1$, and with a 100% completeness for $M_{200c} > 10^{14.6}M_{\odot}$ within the same redshift range. We also found that the YOLO-CL selection function is almost flat with respect to the halo mass up to $z \sim 0.9$. In this section, we discuss how this performance compare with other cluster detection methods in optical imaging surveys and other wavelengths.

At lower redshift than LSST, the current DES covers 5,000 sq. deg. in the g, r, i, z and Y bandpasses and reaches a 10σ depth

at 24.7, 24.4 and 23.8 mag in g, r and i respectively¹⁵. This corresponds to a 5σ depth ~ 2 mag shallower than LSST. The DES redMaPPer cluster catalog (Rykoff et al. 2016) is 100% complete for richness $\lambda > 70$, which corresponds to a halo mass of $M_{200c} \sim 10^{14.8} M_{\odot}$, using weak lensing and X-ray halo mass estimations for redMaPPer clusters (McClintock et al. 2019; Upsdell et al. 2023). Given the large difference in survey depth, it is not surprising that this catalog is less complete than YOLO-CL DC2 catalog at lower masses.

When comparing to predictions for cluster catalogs completeness and purity at the LSST depth, empirical simulations and a Bayesian cluster finder (Ascaso et al. 2012, 2015) predict similar completeness and purity as YOLO-CL (86-98%) in the redshift range $0.5 \lesssim z \lesssim 1.0$ for $M_h > 10^{14.3} M_{\odot}$ (Ascaso et al. 2017), which corresponds to $M_{200c} > 10^{14.24} M_{\odot}$ ¹⁶.

For observational comparisons, the first survey that reached a depth closer to LSST is the Canada-France-Hawaii Telescope Legacy Survey (CFHT-LS)¹⁷ (Gwyn 2012). The median 50% completeness limits in its four deep fields (~ 4 sq. deg.) are 26.3, 26.3 and 25.9 in the g, r, and i bandpasses, respectively (Cabanac et al. 2007). When we analyze the 5σ limit, we obtain similar depths as LSST in these three bands. Several algorithms were applied to the CFHT-LS deep fields to obtain galaxy cluster samples 90-95% complete at $0.2 < z < 0.8$ and 90% pure for clusters with richness $\lambda > 50$ in simulated data (Grove et al. 2009), and 100% complete and 85-90% pure at $M_{200c} > 10^{14.5} M_{\odot}$ (Milkeraitis et al. 2010).

A recent survey that reaches a depth similar to LSST and uses similar optical filters is the Hyper Suprime Camera Strategic Survey Program (HSC-SSP; Aihara et al. 2018), which covers an area of $\sim 1,000$ sq. deg. and reaches a 5σ depth of 26.8 mag and 26.4 mag in the g and i-bandpasses, respectively. The HSC-SSP cluster catalog obtained with the CAMIRA algorithm (Oguri 2014) is 100% and $\sim 90\%$ complete and $\geq 90\%$ pure for $M_{200c} > 10^{14.64} M_{\odot}$ and $M_{200c} > 10^{13.94} M_{\odot}$, respectively, in the redshift range $0.1 \lesssim z \lesssim 1.1$ (Oguri et al. 2018). The CAMIRA algorithm is similar to redMaPPer, and searches for red sequence galaxy overdensities. The WHL09/12 algorithm (Wen et al. 2009, 2012), applied to a compilation of the HSC-SSP and unWISE catalogs, delivers a cluster catalog 100% complete for $M_{200c} > 10^{14.8} M_{\odot}$ (Wen & Han 2021), and 80-90% complete for $M_{200c} > 10^{14.4} M_{\odot}$ at $0.2 \lesssim z \lesssim 1$. The purity of the sample is not discussed. The completeness significantly decreases for lower cluster mass, reaching $\lesssim 70$ -60% completeness for $M_{200c} > 10^{14.1} M_{\odot}$.

When compared to the completeness and purity expected for Euclid cluster catalogs at $z < 1$ (Euclid Collaboration et al. 2019) using simulations from Ascaso et al. (2015), the YOLO-CL DC2 detections are more complete and pure for $M > 10^{14} M_{\odot}$. The best purity and completeness of $\sim 90\%$ at this mass and redshift ranges were obtained with the algorithm AMICO (Bellagamba et al. 2018). The other Euclid cluster finder, PZWav, based on wavelet filtering, gives catalogs ~ 85 -87% complete and pure (Euclid Collaboration et al. 2019).

Overall, the performance of YOLO-CL on DC2 simulations is similar or higher when compared to both current optical surveys at the same depth and redshift range, and LSST and Euclid simulation predictions for future cluster catalogs.

¹⁵ <https://des.ncsa.illinois.edu/releases/dr2>

¹⁶ Hereafter, M_{200c} masses were derived from the original M_h and M_{500} masses found in the literature, using the web-calculator for the equations from Ragagnin et al. (2021), https://c2pacosmosim.uc.lrz.de/static/hydro_mc/webapp/index.html

¹⁷ <https://www.cfht.hawaii.edu/Science/CFHLS/>

To compare with present and future cluster catalogs obtained at other wavelengths, we compare our results with cluster catalogs obtained by the Sunyaev–Zeldovich (SZ; Sunyaev & Zeldovich 1972) effect and X-ray flux measurements, which are both sensitive to the cluster hot gas content.

SZ cluster catalogs are mass-limited and the deepest catalogs available at present reach 100% completeness at $M_{200c} > 10^{14.86} - 10^{14.94} M_{\odot}$ at $z \lesssim 1.5$ from observations with the South Pole Telescope Polarimeter (SPTPol; Bleem et al. 2020), a much higher mass limit than optical and infrared surveys. The SPT-SZ survey (Bleem et al. 2015) catalog is 100% complete at $M_{200c} > 10^{14.94} - 10^{15.00} M_{\odot}$ in a similar redshift range. The cluster catalog obtained from the fifth data release (DR5) of observations ($13,211 \text{ deg}^2$) with the Atacama Cosmology Telescope (ACT) is 90% complete for the clusters with $M_{200c} > 10^{14.76-14.66}$ at $0.2 < z < 2.0$ (Hilton et al. 2021). The Planck space mission PSZ2 all-sky cluster catalog (Planck Collaboration et al. 2016) is 80% complete for $M_{200c} > 10^{14.76} M_{\odot}$ at $0.4 < z < 0.6$, and for $M_{200c} > 10^{14.3} M_{\odot}$ for clusters at $z \sim 0.2$.

Simulations of the current SPT-3G survey, which will provide much deeper observations (Benson et al. 2014), were used to estimate the completeness and purity that can be attained with another deep convolutional neural network (Lin et al. 2021), combined with a classical match filter (Melin et al. 2006). This work shows that $\sim 95\%$ completeness and purity is predicted to be attained at $M_{200c} > 10^{14.7} M_{\odot}$ at $z \gtrsim 0.25$.

This means that all present SZ surveys reach $\sim 95\%$ completeness at cluster masses much higher than what is predicted for LSST from this work. However, the next generation SZ experiments, like SPT-3G, Simons Observatory, CMB-S4 will obtain cluster catalogs with a limiting mass $M_{200c} \sim 10^{14} M_{\odot}$ more comparable to the LSST mass limit (Raghunathan 2022). The CMB-S4 WIDE (Abazajian et al. 2016) survey will reach the S/N=5 cluster detection limit of $M_{200c} = 10^{14.1} M_{\odot}$ at the redshift range $0.2 < z < 1$ over 67% of the sky; the S/N=5 detection threshold for the Simons Observatory (Ade et al. 2019) is planned to be $M_{200c} = 10^{14.3} M_{\odot}$ in the same redshift range over 40% of the sky; and the CMB-S4 ULTRADEEP and CMB-HD (Sehgal et al. 2019) surveys are built to reach up to $M_{200c} = 10^{14} M_{\odot}$ and $M_{200c} = 10^{13.8} M_{\odot}$, respectively. However, the CMB-S4 ULTRADEEP survey covers only 3% of the sky, while CMB-HD is planned to cover $\sim 50\%$ of the sky. All these survey are planned for ≥ 2030 , most probably about at the same time as the the 5-year LSST data release.

For what concerns X-ray surveys, the reference X-ray all-sky cluster catalog is the Röntgensatellit (ROSAT; Pfeiffermann et al. 1987; Voges et al. 1999) catalog of Extended Brightest Cluster Sample (BCS; Ebeling et al. 1998), which contains 201 cluster in Northern hemisphere and is 90% complete for $z < 0.3$ and X-ray fluxes higher than $4.4 \cdot 10^{-12} \text{ erg/cm}^2/\text{s}$. The MCXC cluster catalog (Piffaretti et al. 2011) is a compilation of several catalogs/surveys that consists of ROSAT-based catalogs and serendipitous catalogues, summarized in Table 2. As expected, X-ray surveys detect clusters at much higher masses than LSST at $z=0.5-1$.

The ComPRASS catalog (Tarrío et al. 2019) presents a compilation of Planck (Planck Collaboration et al. 2016) and RASS (Popesso et al. 2004) catalogs of galaxy clusters that were observed in X-ray and using SZ, and reaches deeper than each survey used to compile it. Therefore, the selection function is a complicated combination of the selection function of several surveys. ComPRASS is 100% complete for $M_{200c} > 10^{14.6} M_{\odot}$, $M_{200c} > 10^{14.8} M_{\odot}$, and $M_{200c} > 10^{14.7} M_{\odot}$ at $z < 0.3$ and $z < 0.6$,

Table 2. Completeness of X-ray cluster catalogs. Columns are: 1. Full name of the catalog, 2. Acronym of the catalog, 3. Percentage of the total sky area observed by the survey, 4. Redshift range, 5. Limiting observed flux F_X , 6. Completeness for flux $> F_X$, and 7. M_{200c} mass limit at the median redshift, and at $z=0.5-1$, calculated following Pratt et al. (2009). We indicate the redshift (or the redshift range) in parenthesis.

Name	Acronym	Area % of sky	Redshift range	F_X $erg/cm^2/s$	Comp. %	M_{200c} limit M_\odot
MCXC: ROSAT						
ROSAT-ESO Flux-Limited X-Ray	REFLEX ^a	33	$0 < z < 0.3$	$3 \cdot 10^{-12}$	100	$10^{13.9}$ (0.075) $10^{15.1-15.6}$ (0.5-1)
Northern ROSAT All-Sky Galaxy Cluster Survey	NORAS ^b	41	$0 < z < 0.3$	$3 \cdot 10^{-12}$	50	$10^{13.9}$ (0.075) $10^{15.1-15.6}$ (0.5-1)
ROSAT Brightest Cluster Sample	BCS ^c	41	$0 < z < 0.3$	$4.4 \cdot 10^{-12}$	90	$10^{13.9}$ (0.075) $10^{15.1-15.6}$ (0.5-1)
Catalog of clusters in the region of 1 ster. around the south galactic pole	SGP ^d	8	$0 < z < 0.3$	$3 \cdot 10^{-12}$	100	$10^{13.9}$ (0.075) $10^{15.1-15.6}$ (0.5-1)
ROSAT north ecliptic pole survey	NEP ^e	0.2	$0 < z < 0.8$	$2.0 \cdot 10^{-14}$	100	$10^{13.9}$ (0.200) $10^{14.5-15.0}$ (0.5-1)
Massive Cluster Survey	MACS ^f	55	$0.3 < z < 0.6$	$2 \cdot 10^{-12}$ $< 2 \cdot 10^{-12}$	93 59	$10^{13.9}$ (0.370) $10^{14.5-15.0}$ (0.5-1)
MCXC: Serendipitous surveys						
160 Square Degree ROSAT Survey	160SD ^g	3.8	$0 < z < 0.7$	$1.4 \cdot 10^{-14}$	100	$10^{13.6}$ (0.250) $10^{14.3-14.8}$ (0.5-1)
400 Square Degree ROSAT PSPC Galaxy Cluster Survey	400SD ^h	9.5	$0 < z < 0.7$	$1.4 \cdot 10^{-14}$	100	$10^{13.6}$ (0.200) $10^{14.5-15.0}$ (0.5-1)
Southern Serendipitous High-redshift Archival ROSAT Cluster survey	SHARC ⁱ	0.4	$0 < z < 0.7$	$4.6 \cdot 10^{-14}$	100	$10^{13.6}$ (0.340) $10^{14.5-15.0}$ (0.5-1)
Extended Medium-Sensitivity Survey Distant Cluster Sample	EMSS ^j	1.8	$0 < z < 0.7$	$5 \cdot 10^{-14} \dots 3 \cdot 10^{-12}$	100	$10^{13.6}$ (0.115) $10^{14.5-15.0}$ (0.5-1)
Wide Angle ROSAT Pointed Survey Distant Cluster Sample	WARPS ^k	1.3	$0 < z < 0.9$	$6.5 \cdot 10^{-14}$	100	$10^{13.6}$ (0.284) $10^{14.2-14.7}$ (0.5-1)
eROSITA Final Equatorial-Depth Survey	eFEDS ^l	3.3	$0 < z < 1.3$	$1 \cdot 10^{-14}$	40	$10^{13.8}$ (0.353) $10^{14.1-14.6}$ (0.5-1)
eRASS1 cosmology cluster sample^m		50	$0 < z < 1.3$	$1.6 \cdot 10^{-12}$	80	$10^{14.4}$ (~ 0.300) $10^{14.1-14.6}$ (0.5-1)

^aBohringer et al. (2004); ^bBohringer et al. (2000); ^cEbeling et al. (1998); ^dCraddace et al. (2002); ^eHenry et al. (2006); ^fEbeling et al. (2001); ^gMullis et al. (2003); ^hBurenin et al. (2007); ⁱRomer et al. (2000); ^jBurke et al. (2003); ^kGioia et al. (1990); ^lPerلمان et al. (2002); ^mHorner et al. (2008); ⁿBrunner et al. (2022); ^oMerloni et al. (2024); ^pKluge et al. (2024)

and $0.6 < z < 1.0$, respectively, which are much lower than the completeness limit for the SZ catalogs used to build it.

In conclusion, YOLO-CL shows similar completeness and purity as other algorithms applied to current deep optical imaging surveys like CFHTLS Deep and HSC-SSP, and better completeness and purity than most of the other methods that have been applied to Euclid simulations. Compared to current SZ and X-ray surveys, YOLO-CL can obtain more complete and pure catalogs at much lower masses. However, future SZ surveys are planned to provide much deeper complete and pure catalogs directly comparable with ours. With respect to this, we notice that both SZ surveys and the YOLO-CL selection function are mass-limited, making the SZ-optical comparison based on similar selection functions. YOLO-CL detections can also be combined to SZ and X-ray detections as it was done for the ComPRASS compilation,

to reach catalogs with higher completeness and purity at lower masses.

It has to be noticed that in this paper we focus our analysis on the targeted detections, with the goal to analyze the performance of the algorithm itself, independently of possible systematics and biases introduced by the variations of the parameters of the images generated in a survey mode. In future papers, we will apply YOLO-CL to DC2 images in a survey mode, and our detections will be compared to other LSST cluster detection algorithms applied to the DC2 simulations.

6. Summary

We applied the YOLO-CL deep convolutional network (Grishin et al. 2023) to observations from SDSS and DESC DC2 sim-

ulations to estimate its performance for LSST. We trained the network on 12,203 and 1,171 g, r and i composite color images from SDSS and from the DESC DC2 simulations, respectively, and validated on the same number of cluster images (for a total of 24,406 SDSS and 2,342 DC2 training and validation images) and 6,451 random fields. We conclude that:

- When using DC2 LSST simulated images with a pixel size equal to four times the LSST pixel resolution ($\approx 0.8''/\text{pix}$), the YOLO-CL DC2 cluster catalog is 94% pure and complete for $M_{200c} > 10^{14}M_{\odot}$ and at $0.2 < z < 1$, and 100% complete for $M_{200c} > 10^{14.6}M_{\odot}$.
- The cluster selection function is mass-limited at $0.2 < z < 0.9$.
- When compared to other cluster detection methods in current optical surveys that reach LSST depth and simulations of the Euclid surveys, YOLO-CL shows similar or better completeness and purity.
- Current X-ray and SZ cluster surveys do not reach YOLO-CL completeness and purity at $M_{200c} > 10^{14}M_{\odot}$ and at $0.2 < z < 1$, while future SZ surveys will be directly comparable to LSST YOLO-CL detections and will have similar mass-limited selection functions.

This paper shows that YOLO-CL will permit us to obtain LSST cluster catalogs that will be 94% pure and complete for $M_{200c} > 10^{14}M_{\odot}$ and at $0.2 < z < 1$, and 100% for $M_{200c} > 10^{14.6}M_{\odot}$. The YOLO-CL cluster selection function is mass-limited in the redshift range $0.2 < z < 0.9$. We focused our analysis on targeted detections, with the goal to analyze the performance of the algorithm itself, independently of possible systematics and biases introduced by a survey mode.

We compare our algorithm to other cluster detection methods in current optical surveys that reach LSST depth and simulations of the Euclid surveys, and YOLO-CL shows similar or better completeness and purity. When compared to current X-ray and SZ cluster surveys YOLO-CL reaches higher completeness and purity at $M_{200c} > 10^{14}M_{\odot}$ and at $0.2 < z < 1$. However, future SZ surveys will reach similar completeness and purity at the same depth as LSST YOLO-CL detections, and will have similar mass-limited selection functions.

We note that this analysis was based on LSST DC2 images and did not involve the image processing required to obtain galaxy photometric and photometric redshift catalogs, or the masking of stellar sources and artifacts. The advantage of this deep machine learning approach that works directly on images is to obtain cluster catalogs that will be complementary to other optical detection methods used in the LSST DESC collaboration, and that will be independent from systematic and statistical uncertainties inherent to galaxy catalog production.

In future papers, we will study the YOLO-CL performance in survey mode, and our detections will be compared to other LSST cluster detection algorithms.

Acknowledgements. We thank Université Paris Cité (UPC), which founded KG’s Ph.D. research. We gratefully acknowledge support from the CNRS/IN2P3 Computing Center (Lyon - France) for providing computing and data-processing resources needed for this work. We describe below the author’s contributions. Kirill Grishin applied YOLO-CL to the DC2 simulations, produced the results and figures in the paper, and was the main writer of Sections 2.2 and 5. Simona Mei co-conceived the YOLO-CL network with Stéphane Ilic, developed the content of this paper, supervised the work of Kirill Grishin, Stéphane Ilic and Michel Aguena, and was the main writer of the paper’s text, answered the internal DESC reports. She is the contact with the editor. Stéphane Ilic modified the original YOLO network to adapt it for galaxy cluster detection. He co-conceived YOLO-CL with Simona Mei and developed the network and analysis

software to derive the completeness and purity plots. Michel Aguena contributed to the generation and validation of the DC2 images, and to the analysis and discussion of the cluster detection, including the improvement on the purity estimation model. He also shaped the final image generation software used, and provided the masses and richnesses estimations to the dark matter halo catalog. Dominique Boutigny and Marie Paturel helped with image generation at the beginning of the project and experimented with different versions of YOLO. These statements have been validated with the DESC publication board after having the confirmation of the authors. The Dark Energy Science Collaboration (DESC) acknowledges ongoing support from the IN2P3 (France), the STFC (United Kingdom), and the DOE, NSF, and LSST Corporation (United States). As members of the DESC collaboration, we used resources of the IN2P3 Computing Center (CC-IN2P3–Lyon/Villeurbanne - France) funded by the Centre National de la Recherche Scientifique; the National Energy Research Scientific Computing Center, a DOE Office of Science User Facility supported under Contract No. DE-AC02-05CH11231; STFC DiRAC HPC Facilities, funded by UK BEIS National E-infrastructure capital grants; and the UK particle physics grid, supported by the GridPP Collaboration. This work was performed in part under DOE Contract DE-AC02-76SF00515. This paper has undergone an internal review by the LSST DESC, and we thank the internal reviewers, Camille Avestruz and Markus Michael Rau, for fruitful discussions that improved the paper.

References

- Abazajian, K. N., Adelman-McCarthy, J. K., Agüeros, M. A., et al. 2009, *ApJS*, 182, 543
- Abazajian, K. N., Adshead, P., Ahmed, Z., et al. 2016, arXiv e-prints, arXiv:1610.02743
- Abbott, T. M. C., Abdalla, F. B., Allam, S., et al. 2018, *ApJS*, 239, 18
- Ade, P., Aguirre, J., Ahmed, Z., et al. 2019, *J. Cosmology Astropart. Phys.*, 2019, 056
- Aihara, H., Armstrong, R., Bickerton, S., et al. 2018, *PASJ*, 70, S8
- Angora, G., Rosati, P., Meneghetti, M., et al. 2023, *A&A*, 676, A40
- Ascaso, B., Mei, S., Bartlett, J. G., & Benítez, N. 2017, *MNRAS*, 464, 2270
- Ascaso, B., Mei, S., & Benítez, N. 2015, *MNRAS*, 453, 2515
- Ascaso, B., Wittman, D., & Benítez, N. 2012, *MNRAS*, 420, 1167
- Bayliss, M. B., Hennawi, J. F., Gladders, M. D., et al. 2011, *ApJS*, 193, 8
- Behroozi, P., Wechsler, R. H., Hearin, A. P., & Conroy, C. 2019, *MNRAS*, 488, 3143
- Bellagamba, F., Roncarelli, M., Maturi, M., & Moscardini, L. 2018, *MNRAS*, 473, 5221
- Benson, A. J. 2012, *New A*, 17, 175
- Benson, B. A., Ade, P. A. R., Ahmed, Z., et al. 2014, in *Society of Photo-Optical Instrumentation Engineers (SPIE) Conference Series*, Vol. 9153, Millimeter, Submillimeter, and Far-Infrared Detectors and Instrumentation for Astronomy VII, ed. W. S. Holland & J. Zmuidzinas, 91531P
- Bleem, L. E., Bocquet, S., Stalder, B., et al. 2020, *ApJS*, 247, 25
- Bleem, L. E., Stalder, B., de Haan, T., et al. 2015, *ApJS*, 216, 27
- Bohringer, H., Schuecker, P., Guzzo, L., et al. 2004, *A&A*, 425, 367
- Bohringer, H., Voges, W., Huchra, J. P., et al. 2000, *ApJS*, 129, 435
- Bonjean, V. 2020, *A&A*, 634, A81
- Bosch, J., Armstrong, R., Bickerton, S., et al. 2018, *PASJ*, 70, S5
- Brunner, H., Liu, T., Lamer, G., et al. 2022, *A&A*, 661, A1
- Bruzual, G. & Charlot, S. 2003, *MNRAS*, 344, 1000
- Burenin, R. A., Vikhlinin, A., Hornstrup, A., et al. 2007, *ApJS*, 172, 561
- Burke, D. J., Collins, C. A., Sharples, R. M., Romer, A. K., & Nichol, R. C. 2003, *MNRAS*, 341, 1093
- Cabanaac, R. A., Alard, C., Dantel-Fort, M., et al. 2007, *A&A*, 461, 813
- Chan, M. C. & Stott, J. P. 2019, *MNRAS*, 490, 5770
- Chen, X., Zhu, F., Gaines, S., & Padmanabhan, N. 2023, *MNRAS*, 523, 6272
- Cornu, D. & Montillaud, J. 2021, *A&A*, 647, A116
- Cornu, D., Montillaud, J., Marshall, D. J., Robin, A. C., & Cambrésy, L. 2022, arXiv e-prints, arXiv:2201.05571
- Cruddace, R., Voges, W., Böhringer, H., et al. 2002, *ApJS*, 140, 239
- Davidzon, I., Jegatheesan, K., Ilbert, O., et al. 2022, *A&A*, 665, A34
- Dimauro, P., Huertas-Company, M., Daddi, E., et al. 2018, *MNRAS*, 478, 5410
- Domínguez Sánchez, H., Huertas-Company, M., Bernardi, M., Tuccillo, D., & Fischer, J. L. 2018, *MNRAS*, 476, 3661
- Ebeling, H., Edge, A. C., Böhringer, H., et al. 1998, *MNRAS*, 301, 881
- Ebeling, H., Edge, A. C., & Henry, J. P. 2001, *ApJ*, 553, 668
- Eifer, T., Miyatake, H., Krause, E., et al. 2021, *MNRAS*, 507, 1746
- Euclid Collaboration, Adam, R., Vannier, M., et al. 2019, *A&A*, 627, A23
- Euclid Collaboration, Bisigello, L., Conselice, C. J., et al. 2023a, *MNRAS*, 520, 3529
- Euclid Collaboration, Bretonnière, H., Huertas-Company, M., et al. 2022, *A&A*, 657, A90
- Euclid Collaboration, Humphrey, A., Bisigello, L., et al. 2023b, *A&A*, 671, A99
- Evrard, A. E., Bialek, J., Busha, M., et al. 2008, *ApJ*, 672, 122
- Farahi, A., Chen, X., Evrard, A. E., et al. 2019, *MNRAS*, 490, 3341
- Fioc, M. & Rocca-Volmerange, B. 1999, arXiv e-prints, astro
- Gioia, I. M., Henry, J. P., Maccacaro, T., et al. 1990, *ApJ*, 356, L35
- Girshick, R., Donahue, J., Darrell, T., & Malik, J. 2013, arXiv e-prints, arXiv:1311.2524
- Gladders, M. D. & Yee, H. K. C. 2005, *ApJS*, 157, 1
- Górski, K. M., Hivon, E., Banday, A. J., et al. 2005, *ApJ*, 622, 759
- Grishin, K., Mei, S., & Ilić, S. 2023, *A&A*, 677, A101
- Grove, L. F., Benoist, C., & Martel, F. 2009, *A&A*, 494, 845
- Gwyn, S. D. J. 2012, *AJ*, 143, 38
- Hao, J., McKay, T. A., Koester, B. P., et al. 2010, *ApJS*, 191, 254
- Heitmann, K., Finkel, H., Pope, A., et al. 2019, *ApJS*, 245, 16
- Henghes, B., Pettitt, C., Thyagalingam, J., Hey, T., & Lahav, O. 2021, *MNRAS*, 505, 4847
- Henry, J. P., Mullis, C. R., Voges, W., et al. 2006, *ApJS*, 162, 304
- Hezaveh, Y. D., Perreault Levasseur, L., & Marshall, P. J. 2017, *Nature*, 548, 555
- Hilton, M., Sifón, C., Naess, S., et al. 2021, *ApJS*, 253, 3
- Horner, D. J., Perlman, E. S., Ebeling, H., et al. 2008, *ApJS*, 176, 374
- Huertas-Company, M., Gravit, R., Cabrera-Vives, G., et al. 2015, *ApJS*, 221, 8
- Huertas-Company, M. & Lanusse, F. 2023, *PASA*, 40, e001
- Huertas-Company, M., Primack, J. R., Dekel, A., et al. 2018, *ApJ*, 858, 114
- Hurier, G., Aghanim, N., & Douspis, M. 2021, *A&A*, 653, A106
- Ivezić, Ž., Kahn, S. M., Tyson, J. A., et al. 2019, *ApJ*, 873, 111
- Ivezić, Ž., & the LSST Science Collaboration. 2013, Online article
- Jeffrey, N., Lanusse, F., Lahav, O., & Starck, J.-L. 2020, *MNRAS*, 492, 5023
- Kahn, S. 2018, in 42nd COSPAR Scientific Assembly, Vol. 42, E1.16–5–18
- Kluge, M., Comparat, J., Liu, A., et al. 2024, arXiv e-prints, arXiv:2402.08453
- Knobel, C., Lilly, S. J., Iovino, A., et al. 2009, *ApJ*, 697, 1842
- Koester, B. P., McKay, T. A., Annis, J., et al. 2007, *ApJ*, 660, 239
- Korytov, D., Hearin, A., Kovacs, E., et al. 2019, *ApJS*, 245, 26
- Kovacs, E., Mao, Y.-Y., Agüena, M., et al. 2022, *The Open Journal of Astrophysics*, 5, 1
- Laureijs, R., Amiaux, J., Arduini, S., et al. 2011, arXiv:1110.3193
- Licitra, R., Mei, S., Raichoor, A., Erben, T., & Hildebrandt, H. 2016a, *MNRAS*, 455, 3020
- Licitra, R., Mei, S., Raichoor, A., et al. 2016b, *ApJ*, 829, 44
- Lin, Y.-T., Mohr, J. J., Gonzalez, A. H., & Stanford, S. A. 2006, *ApJ*, 650, L99
- Lin, Z., Huang, N., Avestruz, C., et al. 2021, *MNRAS*, 507, 4149
- LSST Dark Energy Science Collaboration (LSST DESC), Abolfathi, B., Alonso, D., et al. 2021, *ApJS*, 253, 31
- LSST Science Collaboration, Abell, P. A., Allison, J., et al. 2009, arXiv e-prints, arXiv:0912.0201
- Lupton, R., Blanton, M. R., Fekete, G., et al. 2004, *PASP*, 116, 133
- Lupton, R., Gunn, J. E., Ivezić, Z., Knapp, G. R., & Kent, S. 2001, in *Astronomical Society of the Pacific Conference Series*, Vol. 238, *Astronomical Data Analysis Software and Systems X*, ed. J. Harnden, F. R., F. A. Primini, & H. E. Payne, 269
- Mao, Y.-Y., Kovacs, E., Heitmann, K., et al. 2018, *ApJS*, 234, 36
- Maturi, M., Bellagamba, F., Radovich, M., et al. 2019, *MNRAS*, 485, 498
- McClintock, T., Varga, T. N., Gruen, D., et al. 2019, *MNRAS*, 482, 1352
- Mei, S., Scarlata, C., Pentericci, L., et al. 2015, *ApJ*, 804, 117
- Melchior, P., Sheldon, E., Drlica-Wagner, A., et al. 2016, *Astronomy and Computing*, 16, 99
- Melin, J. B., Bartlett, J. G., & Delabrouille, J. 2006, *A&A*, 459, 341
- Merloni, A., Lamer, G., Liu, T., et al. 2024, *A&A*, 682, A34
- Milkeraitis, M., van Waerbeke, L., Heymans, C., et al. 2010, *MNRAS*, 406, 673
- Moskowitz, I., Gawiser, E., Crenshaw, J. F., et al. 2024, *ApJ*, 967, L6
- Mullis, C. R., McNamara, B. R., Quintana, H., et al. 2003, *ApJ*, 594, 154
- Muzzin, A., Wilson, G., Yee, H. K. C., et al. 2012, *ApJ*, 746, 188
- Oguri, M. 2014, *MNRAS*, 444, 147
- Oguri, M., Lin, Y.-T., Lin, S.-C., et al. 2018, *PASJ*, 70, S20
- Oke, J. B. & Gunn, J. E. 1983, *ApJ*, 266, 713
- Olivier, S. S., Riot, V. J., Gilmore, D. K., et al. 2012, in *Society of Photo-Optical Instrumentation Engineers (SPIE) Conference Series*, Vol. 8446, *Ground-based and Airborne Instrumentation for Astronomy IV*, ed. I. S. McLean, S. K. Ramsay, & H. Takami, 84466B
- Olivier, S. S., Seppala, L., Gilmore, K., Hale, L., & Whistler, W. 2006, in *Society of Photo-Optical Instrumentation Engineers (SPIE) Conference Series*, Vol. 6273, *Society of Photo-Optical Instrumentation Engineers (SPIE) Conference Series*, ed. E. Atad-Ettinger, J. Antebi, & D. Lemke, 62730Y
- Parroni, C., Mei, S., Erben, T., et al. 2017, *ApJ*, 848, 114
- Pasquet, J., Bertin, E., Treyer, M., Arnouts, S., & Fouchez, D. 2019, *A&A*, 621, A26
- Perlman, E. S., Horner, D. J., Jones, L. R., et al. 2002, *ApJS*, 140, 265
- Pfeffermann, E., Briel, U. G., Hippmann, H., et al. 1987, in *Society of Photo-Optical Instrumentation Engineers (SPIE) Conference Series*, Vol. 733, *Soft X-ray optics and technology*, ed. E. Koch & G. A. Schmahl, 519
- Piffaretti, R., Arnaud, M., Pratt, G. W., Pointecouteau, E., & Melin, J. B. 2011, *A&A*, 534, A109
- Planck Collaboration, Ade, P. A. R., Aghanim, N., et al. 2016, *A&A*, 594, A27
- Poppo, P., Böhringer, H., Brinkmann, J., Voges, W., & York, D. G. 2004, *A&A*, 423, 449
- Pratt, G. W., Croston, J. H., Arnaud, M., & Böhringer, H. 2009, *A&A*, 498, 361
- Press, W. H. & Schechter, P. 1974, *ApJ*, 187, 425
- Ragagnin, A., Saro, A., Singh, P., & Dolag, K. 2021, *MNRAS*, 500, 5056
- Raghunathan, S. 2022, *ApJ*, 928, 16
- Redmon, J., Divvala, S., Girshick, R., & Farhadi, A. 2015, arXiv e-prints, arXiv:1506.02640
- Redmon, J. & Farhadi, A. 2016, arXiv e-prints, arXiv:1612.08242
- Redmon, J. & Farhadi, A. 2018, arXiv e-prints, arXiv:1804.02767
- Rezatofighi, H., Tsoi, N., Gwak, J., et al. 2019
- Robitaille, T., Deil, C., & Ginsburg, A. 2020, reproject: Python-based astronomical image reprojection, *Astrophysics Source Code Library*, record ascl:2011.023
- Romer, A. K., Nichol, R. C., Holden, B. P., et al. 2000, *ApJS*, 126, 209
- Roodman, A., Bogart, J. R., Bond, T., et al. 2018, in *Society of Photo-Optical Instrumentation Engineers (SPIE) Conference Series*, Vol. 10705, *Modeling, Systems Engineering, and Project Management for Astronomy VIII*, ed. G. Z. Angeli & P. Dierickx, 107050D
- Rowe, B. T. P., Jarvis, M., Mandelbaum, R., et al. 2015, *Astronomy and Computing*, 10, 121
- Roza, E., Rykoff, E. S., Koester, B. P., et al. 2009, *ApJ*, 703, 601
- Rykoff, E. S., Koester, B. P., Roza, E., et al. 2012, *ApJ*, 746, 178
- Rykoff, E. S., Roza, E., Busha, M. T., et al. 2014, *ApJ*, 785, 104

- Rykoff, E. S., Rozo, E., Hollowood, D., et al. 2016, *ApJS*, 224, 1
- Sehgal, N., Aiola, S., Akrami, Y., et al. 2019, in *Bulletin of the American Astronomical Society*, Vol. 51, 6
- Simet, M., McClintock, T., Mandelbaum, R., et al. 2017, *MNRAS*, 466, 3103
- Sirianni, M., Jee, M. J., Benítez, N., et al. 2005, *PASP*, 117, 1049
- Sobral, D., Best, P. N., Geach, J. E., et al. 2010, *MNRAS*, 404, 1551
- Sunyaev, R. A. & Zeldovich, Y. B. 1972, *Comments on Astrophysics and Space Physics*, 4, 173
- Szabo, T., Pierpaoli, E., Dong, F., Pipino, A., & Gunn, J. 2011, *ApJ*, 736, 21
- Tarrío, P., Melin, J. B., & Arnaud, M. 2019, *A&A*, 626, A7
- The LSST Dark Energy Science Collaboration, Mandelbaum, R., Eifler, T., et al. 2018, arXiv e-prints, arXiv:1809.01669
- Upsdell, E. W., Giles, P. A., Romer, A. K., et al. 2023, *MNRAS*, 522, 5267
- Voges, W., Aschenbach, B., Boller, T., et al. 1999, *A&A*, 349, 389
- Wen, Z. L. & Han, J. L. 2021, *MNRAS*, 500, 1003
- Wen, Z. L., Han, J. L., & Liu, F. S. 2009, *ApJS*, 183, 197
- Wen, Z. L., Han, J. L., & Liu, F. S. 2012, *ApJS*, 199, 34
- Werner, S. V., Cypriano, E. S., Gonzalez, A. H., et al. 2023, *MNRAS*, 519, 2630
- Wylezalek, D., Galametz, A., Stern, D., et al. 2013, *ApJ*, 769, 79
- Wylezalek, D., Vernet, J., De Breuck, C., et al. 2014, *ApJ*, 786, 17
- Yoachim, P., Coughlin, M., Angeli, G. Z., et al. 2016, in *Society of Photo-Optical Instrumentation Engineers (SPIE) Conference Series*, Vol. 9910, *Observatory Operations: Strategies, Processes, and Systems VI*, ed. A. B. Peck, R. L. Seaman, & C. R. Benn, 99101A
- York, D. G., Adelman, J., Anderson, John E., J., et al. 2000, *AJ*, 120, 1579
- Zanisi, L., Huertas-Company, M., Lanusse, F., et al. 2021, *MNRAS*, 501, 4359